Title
Dynamics near equilibrium for intense beams in a nonlinear integrable focusing channel

Journal
Journal of Instrumentation, 15(07)

ISSN
1748-0221

Authors
Mitchell, C
Hwang, K
Ryne, R

Publication Date
2020-07-01

DOI
10.1088/1748-0221/15/07/p07019

Peer reviewed

Prepared for submission to JINST

ICFA Beam Dynamics Newsletter
May 2020

Dynamics Near Equilibrium for Intense Beams in a Nonlinear Integrable Focusing Channel

C. Mitchell, K. Hwang, and R. Ryne

Lawrence Berkeley National Laboratory,
1 Cyclotron Road, Berkeley, CA 94720, USA

E-mail: ChadMitchell@lbl.gov

Abstract: Accelerator storage ring designs based on nonlinear integrable Hamiltonian systems provide a novel test-bed for studying the interplay between nonlinear dynamics and space charge at high intensity. In this work, the structure of beam Vlasov equilibria is explored for a constant focusing channel based on the nonlinear focusing potential of the Integrable Optics Test Accelerator. The dynamics of the single-particle orbits is explored in the combined space charge and external focusing fields as a function of beam current, and the self-consistent relaxation of a mismatched beam to equilibrium is characterized.

Keywords: Beam dynamics, accelerator modeling and simulations (multi-particle dynamics)

[1]Corresponding author.

Contents

1 Introduction

In the study of intense charged particle beams in an accelerator storage ring or circular collider, a constant focusing model approximates the beam as a non-neutral plasma confined by a set of applied static focusing fields, which are related to the fields of the true periodic lattice through an appropriate form of averaging [1]. Such models have been used to study successfully several qualitative features of beam dynamics at high intensity, including the structure of Vlasov equilibria [2, 3], the stability/instability of collective space charge modes [4], and the mechanisms of beam halo formation [5, 6]. While such models typically assume the presence of linear external focusing forces, the purpose of this article is to address novel features of the beam dynamics that occur in strongly nonlinear constant focusing channels of a particular type.

The example considered is based on the Integrable Optics Test Accelerator (IOTA), a storage ring at Fermi National Accelerator Laboratory designed (in part) to investigate the dynamics of beams in the presence of highly nonlinear transverse focusing fields that generate integrable single-particle motion with large intrinsic betatron tune spreads ($\Delta\nu_{x,y} > 0.25$) [7, 8]. A primary experimental goal is to determine the degree to which the decoherence of transverse oscillations may be used to mitigate the development of instabilities [9] and core-halo resonances at high space charge intensity [10, 11]. Integrability of the single-particle Hamiltonian motion is enforced by design to improve the transverse dynamic aperture and beam confinement [7, 12].

In Section 2, a constant focusing channel based on the nonlinear focusing of the IOTA storage ring is introduced. In Section 3, the associated Vlasov equilibria are explored. In Section 4, the regularity of single-particle orbits within the equilibrium beam is examined. In Section 5, we study the relaxation of an initially mismatched beam to equilibrium through the mechanism of nonlinear phase mixing. A conclusion follows.

2 A Nonlinear Integrable Focusing Channel

We consider an unbunched, coasting, monoenergetic beam confined transversely by a strongly nonlinear focusing potential similar to that used in the Integrable Optics Test Accelerator at Fermi National Accelerator Laboratory [7, 8]. In particular, consider a constant focusing channel in which motion is described by the Hamiltonian:

$$H = \frac{1}{2}(p_x^2 + p_y^2) + \frac{1}{2}(k_x^2 x^2 + k_y^2 y^2) - \frac{\tau c^2}{\beta}\mathcal{U}\left(\frac{x}{c\sqrt{\beta}}, \frac{y}{c\sqrt{\beta}}\right) + \frac{q\phi(x, y, s)}{\beta_0^2 \gamma_0^3 m c_0^2}. \tag{2.1}$$

Here s (path length) is the independent variable, $k_x = k_y = 1/\beta$, β [m], c [$\mathrm{m}^{1/2}$], and τ [unitless] are constants, and $\mathcal{U}$ is the function:

$$\mathcal{U}(\zeta, \eta) = \mathcal{R}e\left(\frac{z}{\sqrt{1 - z^2}} \arcsin(z)\right), \quad z = \zeta + i\eta. \tag{2.2}$$

In this model, β denotes the beta function of the bare linear focusing (the focusing when $\tau = 0$ and $\phi = 0$), the relativistic factors contain a subscript 0 to distinguish them from the constants β and c, and all momenta are normalized by the design momentum $p^0 = \beta_0 \gamma_0 m c_0$. The beam is assumed to be longitudinally uniform, and in the laboratory frame the (2D) space charge potential ϕ satisfies:

$$\nabla^2 \phi = -\frac{\rho}{\epsilon_0}, \qquad \phi|_{\partial\Omega} = 0, \tag{2.3}$$

where $\partial\Omega$ denotes the transverse conducting boundary. In the special case that $\phi = 0$, the Hamiltonian (2.1) describes integrable motion, admitting two independent invariants of motion of the form [7, 13]:

$$H_N = \frac{1}{2}(p_{xN}^2 + p_{yN}^2 + x_N^2 + y_N^2) - \tau\mathcal{U}(x_N, y_N), \tag{2.4a}$$

$$I_N = (x_N p_{yN} - y_N p_{xN})^2 + p_{xN}^2 + x_N^2 - \tau\mathcal{W}(x_N, y_N), \tag{2.4b}$$

where

$$\mathcal{W}(x_N, y_N) = \mathcal{R}e\left(\frac{z + z^*}{\sqrt{1 - z^2}} \arcsin(z)\right), \quad z = x_N + i y_N \tag{2.5}$$

and

$$x_N = \frac{x}{c\sqrt{\beta}}, \quad y_N = \frac{y}{c\sqrt{\beta}}, \quad p_{xN} = \frac{\sqrt{\beta} p_x}{c}, \quad p_{yN} = \frac{\sqrt{\beta} p_y}{c}. \tag{2.6}$$

One may verify that $\{H_N, I_N\} = 0$, where $\{\cdot, \cdot\}$ denotes the classical Poisson bracket.

Table 1 contains the basic parameters appearing in (2.1) that are used throughout this paper. The proton beam kinetic energy, the nonlinear insert strength τ, and the scale parameter c are chosen to correspond to those used in the IOTA ring design [8]. The parameter β is given by $\beta = C/\Delta\psi$, where $C = 39.97$ m is the IOTA ring circumference and $\Delta\psi = 31.4$ rad denotes the horizontal/vertical phase advance per turn. For simplicity, we take the spatial domain to be rectangular with the half-aperture $a = b$. Finally, the dimensionless quantity $\langle H_N \rangle$ characterizes the size of the beam in its 4D phase space. The corresponding beam emittances are slightly larger than the values $\epsilon_{x,n} = \epsilon_{y,n} = 0.3$ μm provided in [8].

Table 1. Table of parameters for a nonlinear focusing channel (2.1) modeled on the IOTA nonlinear potential for high-intensity proton beam operation.

Parameter	Value	Unit
$(\gamma_0 - 1)mc_0^2$	2.5	MeV
τ	-0.4	-
c	0.01	$\mathrm{m}^{1/2}$
β	1.27	m
a, b	1.69	cm
$\langle H_N \rangle$	0.125	-
$\epsilon_{x,n}, \epsilon_{y,n}$	0.4, 0.8	μm

3 Vlasov Equilibria

We search for stationary solutions of the Vlasov-Poisson system associated with (2.1) in the form:

$$f(x, p_x, y, p_y) = f_0 e^{-H(x,p_x,y,p_y)/H_0}, \quad \int f(x, p_x, y, p_y) dx dp_x dy dp_y = 1, \tag{3.1}$$

where f_0 is a normalization constant. The space charge potential ϕ appearing in H must satisfy (2.3) to ensure self-consistency, which gives:

$$\nabla^2 \phi = -\frac{I}{\epsilon_0 \beta_0 c_0} \int f(x, p_x, y, p_y) dp_x dp_y, \quad \phi|_{\partial\Omega}, \tag{3.2}$$

where I denotes the beam current and ϵ_0 is the permittivity of free space. The resulting system (3.1-3.2) is solved using the spectral Galerkin method described in [14], which yields ϕ as a superposition of 2D Fourier modes. The parameter H_0 is chosen to produce a specified value of $\langle H_N \rangle$, which results in the emittance values provided in Table 1.

Figure 1 shows contours of the spatial projection of the equilibrium density (3.1) for increasing values of the beam current I. In each case, the potential ϕ is computed using 15×15 modes. At zero current, the contours coincide with the equipotentials of the external focusing terms in (2.1). Note that the focusing potential has singular points at $(x_N, y_N) = (\pm 1, 0)$, which provide strong horizontal confinement. As the current is increased (for fixed $\langle H_N \rangle$), the beam size increases in the vertical direction, and the "hourglass" shape of the contours is enhanced. At high intensity, the density maximum in the beam center splits into two distinct maxima.

To verify that the phase space density f in (3.1) is stationary, a beam consisting of 1 M particles was sampled from f and tracked self-consistently according to the Hamiltonian (2.1) using the code IMPACT-Z [15]. A second-order symplectic integrator [16] was used for numerical integration in s, with stepsize $\Delta s = 0.0014\beta$. At each step in s, the solution of the Poisson equation (2.3) for the space charge potential ϕ is obtained from the particle data at s using the gridless spectral algorithm described in [17] on the rectangular domain $[-a, a] \times [-b, b]$.

Figure 2 illustrates the horizontal and vertical density profiles (projections) for the three values of beam current used in Fig. 1. The initial profiles coincide with the profiles obtained after tracking for distance $s = 140\beta$. Note the depression appearing in the vertical beam profile near $y = 0$,

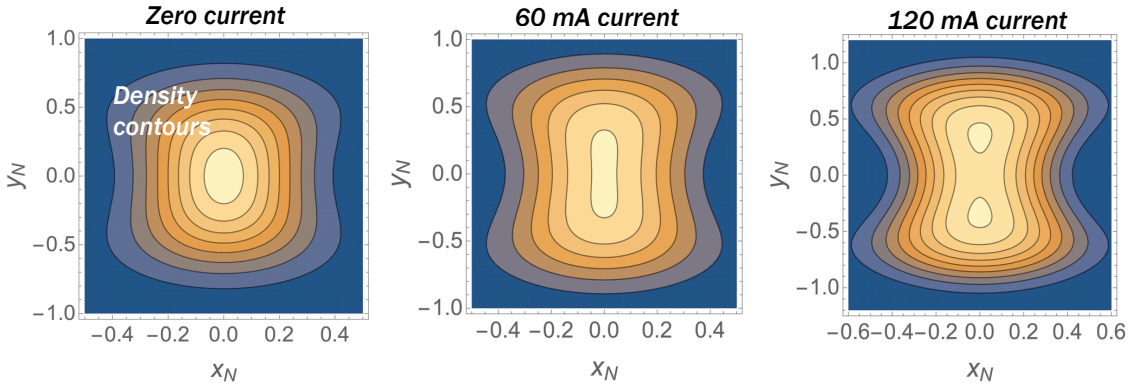

Figure 1. Contours of the spatial projection of the equilibrium phase space density (3.1) obtained for a 2.5 MeV proton beam with current $I = 0$ (left), $I = 60.7$ mA (center), and $I = 120$ mA (right) in a constant focusing channel described by (2.1) for the parameters in Table 1.

which becomes more pronounced with increasing intensity. For the case $I = 60$ mA, each of the four density profiles along (x, p_x, y, p_y) remains visibly stationary over a propagation distance of $s = 2000\beta$, corresponding to 318 (undepressed) betatron periods of the bare linear focusing. (See Fig. 5 of [14].)

4 Single-Particle Orbits

The spectral Galerkin code [14] described in the previous section generates as additional output the 2D Fourier coefficients c_{lm} of the space charge potential of the equilibrium beam. Single-particle orbits may then be tracked using the Hamiltonian (2.1), where ϕ is represented as a time-independent sum of modes:

$$\phi(x, y) = \sum_{l=1}^{l_{\max}} \sum_{m=1}^{m_{\max}} \frac{c_{lm}}{\sqrt{ab}} \sin\left(\frac{l\pi}{2a}(x + a)\right) \sin\left(\frac{m\pi}{2b}(y + b)\right). \tag{4.1}$$

This reduces the computing time required to study the long-term orbit behavior, eliminating the need to perform a costly space charge computation on each time step. In addition, the space charge potential in (4.1) is smooth and free of particle noise. (The error in the potential (4.1) is determined by the initial solution of the nonlinear PDE, which is dominated by the truncation of the Fourier sum. Here $l_{\max} = m_{\max} = 15$.) As a benchmark, we used this procedure to track 1M particles sampled from the equilibrium distribution (3.1). This results in stationary density profiles similar to those shown in Fig. 2.

Figure 3 illustrates the sum of the external focusing potential and the equilibrium space charge potential in the dimensionless form (after scaling by β/c^2):

$$V(x_N, y_N) = \frac{1}{2}(x_N^2 + y_N^2) - \tau \mathcal{U}(x_N, y_N) + \frac{\beta}{c^2}\left[\frac{q\phi(x, y)}{\beta_0^2 \gamma_0^3 m c_0^2}\right]. \tag{4.2}$$

Note that the potential flattens near the origin with increasing intensity, as expected. To characterize

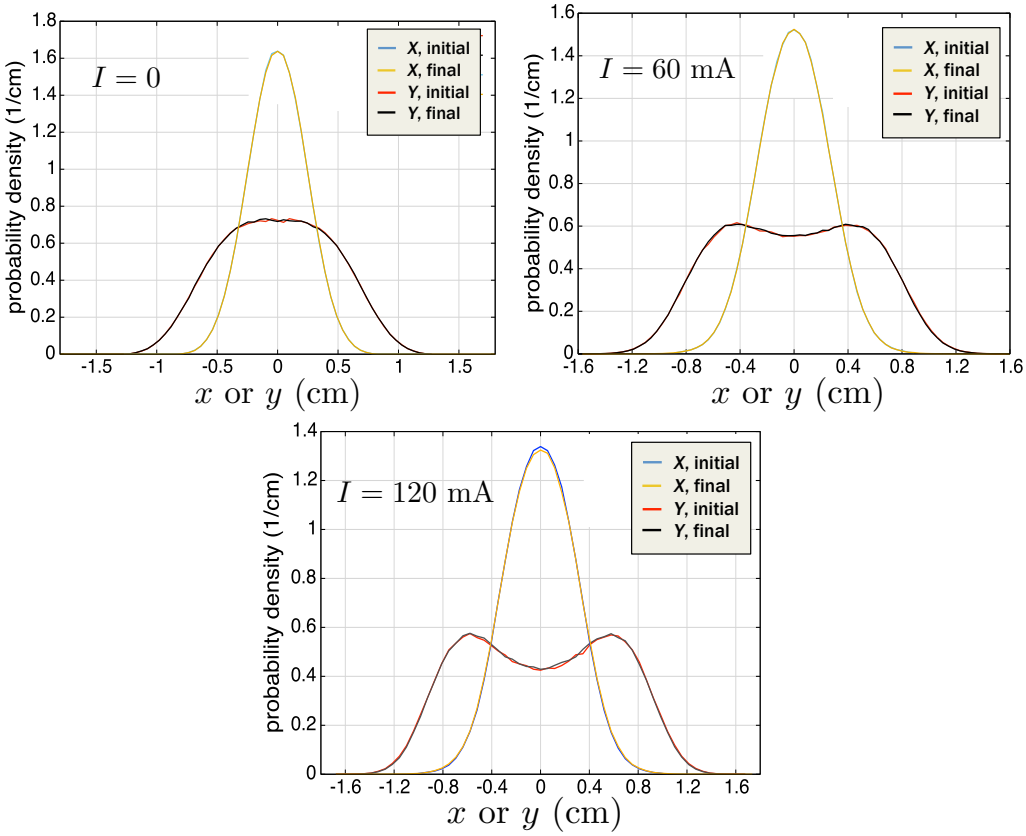

Figure 2. Horizontal and vertical density profiles of a 2.5 MeV proton beam in equilibrium (3.1), given before and after tracking a distance $L = 140\beta$ in the constant focusing channel (2.1). The curves corresponding to the initial and final profiles coincide.

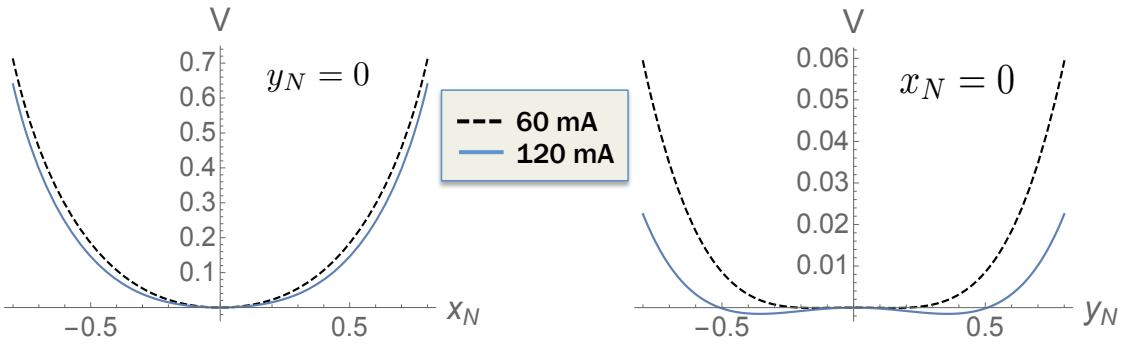

Figure 3. Lineout of the total potential formed by the sum of the external potential and the equilibrium space charge potential for the cases $I = 60$ mA and $I = 120$ mA. (Left) Along the horizontal line $y_N = 0$. (Right) Along the vertical line $x_N = 0$. Note the presence of two minima in the case $I = 120$ mA.

this effect, one may expand (4.2) to obtain terms of second degree in x_N and y_N:

$$V^{(2)}(x_N, y_N) = \frac{1}{2}Ax_N^2 + \frac{1}{2}By_N^2 + Cx_N y_N. \tag{4.3}$$

The coefficients A, B, and C were obtained numerically using (4.1-4.2) for the three cases considered here, and these are provided in Table 2. Since $C \approx 0$, horizontal (vertical) motion is stable near the origin when $A > 0$ ($B > 0$) with betatron frequency $\omega_x \propto \sqrt{A}$ ($\omega_y \propto \sqrt{B}$). Thus, we see that:

$$\frac{\Delta\omega_x}{\omega_{x,0}} = \begin{cases} -0.24 & \text{for } I = 60 \text{ mA}, \\ -0.40 & \text{for } I = 120 \text{ mA}, \end{cases} \tag{4.4}$$

where $\omega_{x,0}$ denotes the frequency in the absence of space charge and $\Delta\omega_x$ denotes the change in frequency at nonzero current. This analysis does not apply to the vertical motion near the origin, which is unstable when $I \geq 60$ mA. (Note, however, that stable fixed points exist away from the origin.)

Table 2. Quadratic part (4.3) of the total focusing potential (4.2). The computed value of C satisfies $|C| < 10^{-12}$, as expected from the symmetry of the external potential under the reflections $x_N \mapsto -x_N$, $y_N \mapsto -y_N$.

	0 mA	60 mA	120 mA
A	1.8	1.048	0.648
B	0.2	-0.009	-0.052
C	0.0	0.0	0.0

A key question regarding the dynamics of beams in nonlinear integrable focusing channels is the relationship between integrability of the single-particle motion and the presence of space charge at high intensity. To explore this, 8K distinct initial conditions of the form $(x, 0, y, 0)$ were sampled from a disk of radius 1.5 cm. Orbits were tracked in the sum of the external potential and the equilibrium space charge potential ϕ for a distance $s = 2903\beta$ (462 betatron periods). Figure 4 illustrates the result of applying NAFF to characterize the rate of tune diffusion D, which is characterized by:

$$D = \log_{10}\sqrt{\Delta\nu_x^2 + \Delta\nu_y^2}, \tag{4.5}$$

where $\Delta\nu_x$ ($\Delta\nu_y$) denotes the change in horizontal (vertical) tune computed over two successive intervals of distance $s = 1451\beta$.

In each case, there exists a region surrounding the origin (blue) that consists of initial conditions with regular orbits. This region fills the entire disk when $I = 0$ (the motion is integrable), and shrinks with increasing current. In particular, there exists a mixture of regular and chaotic orbits within the equilibrium beam (whose boundary is indicated by the white curve). Despite the presence of chaotic orbits, note that the motion is bounded due to the fact that (2.1) is a conserved quantity satisfying:

$$\lim_{|(x,p_x,y,p_y)|\to\infty} H(x, p_x, y, p_y) = +\infty, \tag{4.6}$$

so that no particle with finite energy can escape to infinity.

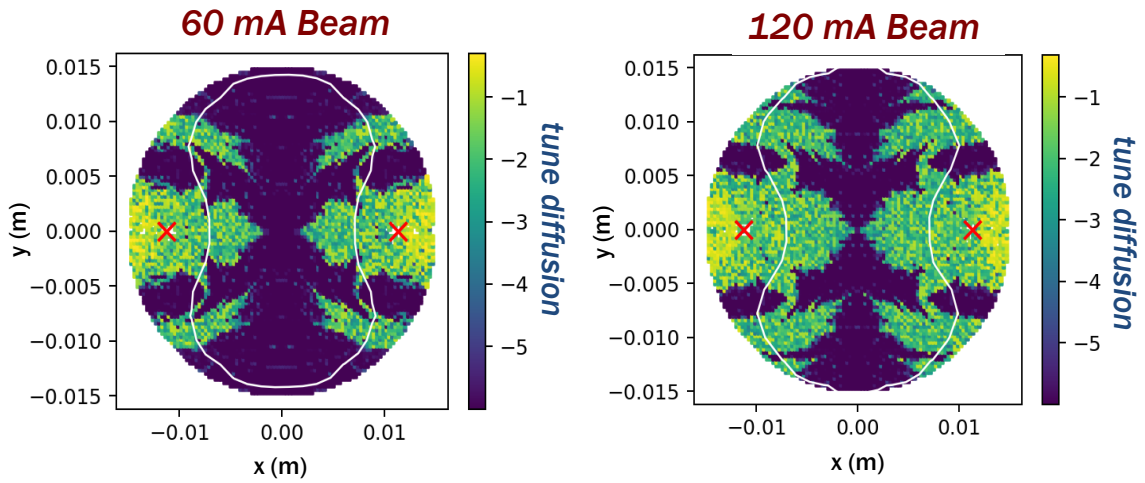

Figure 4. Regions of regular and chaotic motion. The white curve illustrates the boundary of the equilibrium beam. The red crosses denote the two singular points of the nonlinear potential, located at $(x, y) = (\pm 1.13, 0)$ cm.

5 Dynamics of Relaxation

In this section, we consider the dynamics of a beam that is initially mismatched to the nonlinear focusing channel. To introduce mismatch, we generate a beam with a distribution of the form (3.1) that is matched to an incorrect value of current. Figure 5 illustrates the evolution of the rms beam sizes and emittances for a beam that is in equilibrium at $I = 0$, but which is propagated at $I = 60$ mA. Initially, the mismatch induces fluctuations of rms beam size as large as 30%, but both beam sizes and emittances appear to equilibrate within 20 betatron periods. This approach to equilibrium is driven primarily by rapid filamentation of the beam phase space that is caused by nonlinear phase mixing in the external potential, an effect which is seen most clearly in the vertical phase space (Fig. 6).

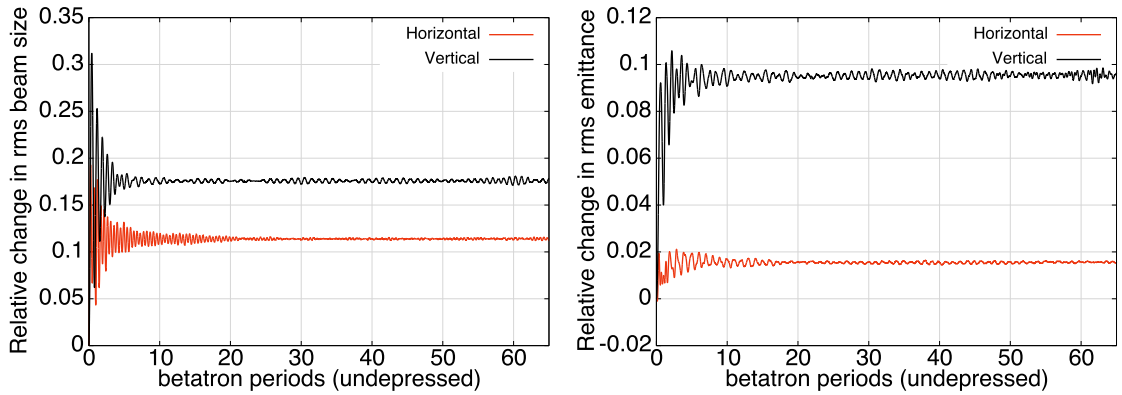

Figure 5. Relaxation to equilibrium of beam sizes and emittances in the nonlinear integrable focusing channel (2.1).

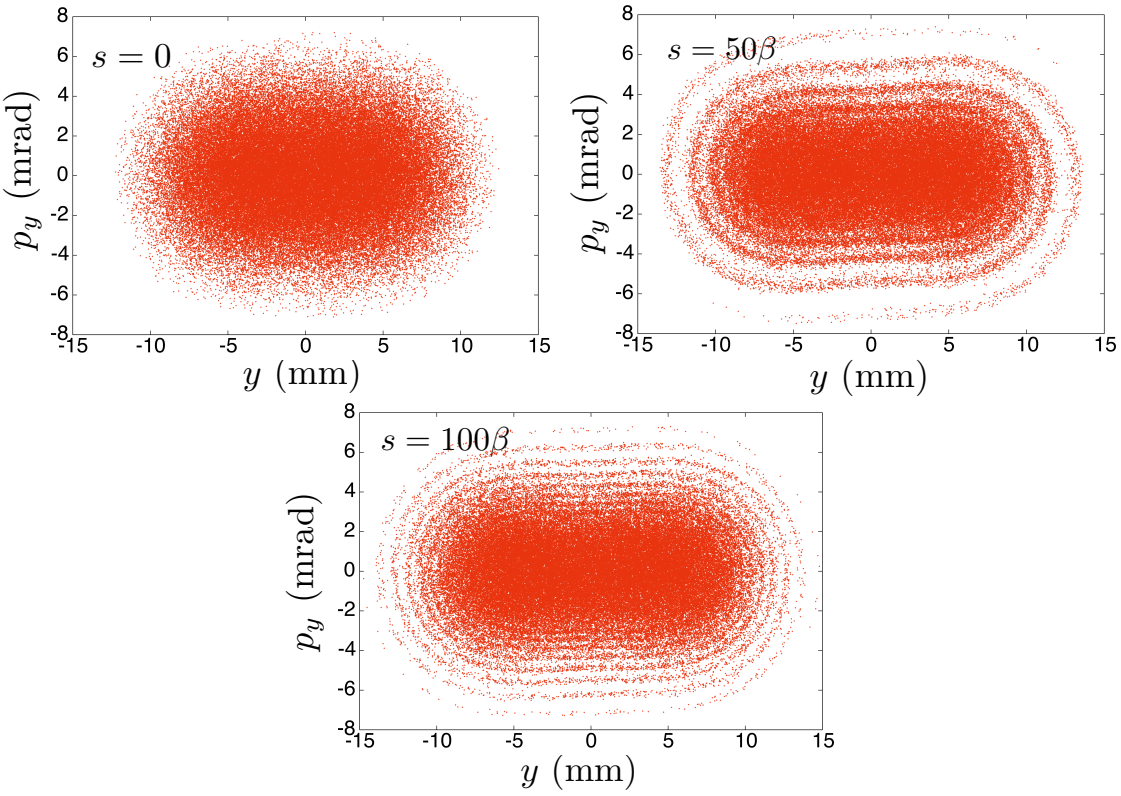

Figure 6. Vertical phase space of a mismatched beam relaxing to equilibrium in the channel (2.1) with $I = 60$ mA, showing filamentation due to strongly nonlinear external focusing.

Figure 7 (left) shows the beam density profiles obtained after tracking this beam for a distance $s = 140\beta$. After tracking, both the horizontal and vertical beam size are increased, and a depression has appeared in the vertical beam profile, characteristic of the equilibrium at $I = 60$ mA. For comparison (right), we have shown the density profiles of the equilibrium beam at $I = 60$ mA. After tracking over the same distance at the mismatched current $I = 0$, the horizontal and vertical beam size are reduced, and the depression in the vertical beam profile has appeared. This suggests that a beam sufficiently near an equilibrium of the form (3.1) relaxes to equilibrium on a time scale $s \sim 100\beta$, and that reversible transitions between two Vlasov equilibria may in some cases be observed by modifying the beam current.

6 Conclusion

Several features of the dynamics of beams in a nonlinear integrable focusing channel were investigated. The Vlasov equilibria can be determined, and these equilibria possess features not observed in the case of linear external focusing, including the appearance of local density minima and unusual density contours. (See [18] for additional examples.) At high intensity, the presence of space charge leads to a mixture of (bounded) regular and chaotic orbits within the equilibrium beam, and the

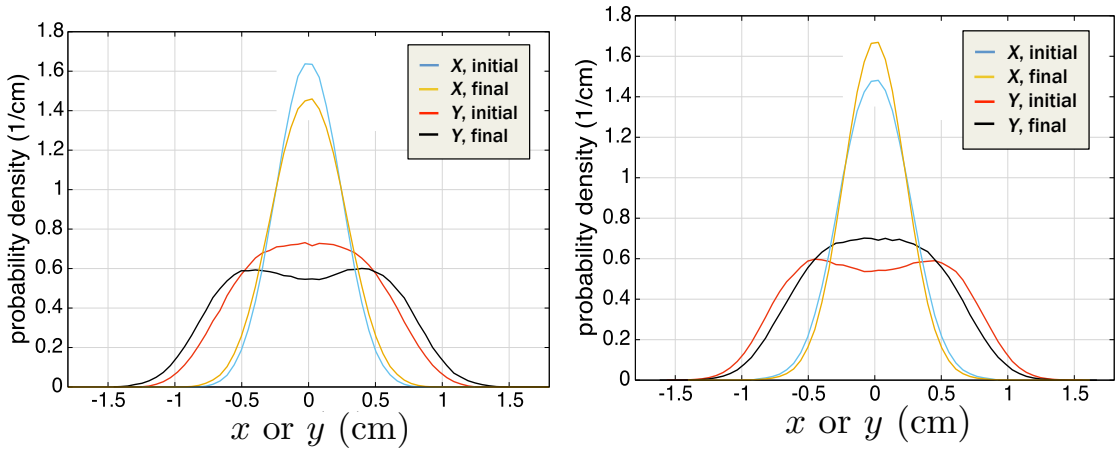

Figure 7. Evolution of the density profiles in x and y for a 2.5 MeV proton beam, given before and after tracking a distance $s = 140\beta$ in the constant focusing channel (2.1) at an unmatched current, showing transition to equilibrium. (Left) A beam in equilibrium at $I = 0$, tracked using $I = 60$ mA. (Right) A beam in equilibrium at $I = 60$ mA, tracked using $I = 0$.

strong nonlinearity of the external focusing fields drives rapid relaxation to Vlasov equilibrium. Such dynamics might also be studied using intense beams in nonlinear Paul traps [19].

The external focusing potential considered here has the property that it increases without bound as $|(x, y)| \to \infty$, so that orbits are spatially confined. It is of interest to determine how these qualitative features change in the presence of an integrable potential without this property. In addition, to what extent do these results generalize to the case of bunched beams in an integrable 3D focusing potential? Finally, work is ongoing to determine which of these qualitative features persist in the presence of a realistic focusing lattice with periodic s-dependence.

Acknowledgments

The authors thank the IOTA collaboration at Fermilab for discussions. This work was supported by the Director, Office of Science of the U.S. Department of Energy under Contract No. DE-AC02-05CH11231, and made use of computer resources at the National Energy Research Scientific Computing Center. The authors acknowledge support from the U.S. DOE Early Career Research Program under the Office of High Energy Physics.

References

[1] R. Davidson and H. Qin, *Physics of Intense Charged Particle Beams in High Energy Accelerators*, Imperial College Press and World Scientific Publishing Co., London (2001).

[2] M. Reiser, *Theory and Design of Charged Particle Beams*, 2nd ed, Wiley-VCH, Weinheim (2008).

[3] S. M. Lund, T. Kikuchi, and R. C. Davidson, *Generation of initial kinetic distributions for simulation of long-pulse charged particle beams with high space-charge intensity*, *Phys. Rev. ST Accel. Beams* **12** (2009) 114801.

[4] M. Venturini and R. Gluckstern, *Resonance analysis for a space charge dominated beam in a circular lattice*, *Phys. Rev. ST Accel. Beams* **3** (2000) 034203.

[5] R. L. Gluckstern, *Analytic model for halo formation in high current ion linacs*, *Phys. Rev. Lett.* **73** (1994) 1247.

[6] J. Qiang and R. Ryne, *Beam halo studies using a three-dimensional particle-core model*, *Phys. Rev. ST Accel. Beams* **3** (2000) 064201.

[7] V. Danilov and S. Nagaitsev, *Nonlinear accelerator lattices with one and two analytic invariants*, *Phys. Rev. ST Accel. Beams* **13** (2010) 084002.

[8] S. Antipov *et al*, *IOTA (Integrable Optics Test Accelerator): facility and experimental beam physics program*, *JINST* **12** (2017) T03002.

[9] E. Stern *et al*, *Suppression of instabilities generated by an anti-damper with a nonlinear magnet element in IOTA*, in *Proceedings of the 9th International Particle Accelerator Conference*, Vancouver, Canada (2018) THPAF068.

[10] S. Webb *et al*, *Suppressing transverse beam halo with nonlinear magnetic fields*, FERMILAB-PUB-294-AD-APC (2012).

[11] S. Webb *et al*, *Effects of nonlinear decoherence on halo formation*, arXiv:1205.7083v2 [physics.acc-ph] (2013).

[12] K. G. Sonnad and J. R. Cary, *Finding a nonlinear lattice with improved integrability using Lie transform perturbation theory*, *Phys. Rev. E* **69** (2004) 056501.

[13] C. Mitchell, *Complex representation of potentials and fields for the nonlinear magnetic insert of the Integrable Optics Test Accelerator*, LBNL-1007217, arXiv:1908.00036 [physics.acc-ph] (2017).

[14] C. Mitchell, R. Ryne, and K. Hwang, *Spectral Galerkin solver for intense beam Vlasov equilibria in nonlinear constant focusing channels*, *Phys. Rev. E* **100** (2019) 053308.

[15] J. Qiang, R. Ryne, S. Habib, and V. Decyk, *An object-oriented parallel particle-in-cell code for beam dynamics simulation in linear accelerators*, *J. Comput. Phys.* **163** (2000) 434.

[16] C. Mitchell and J. Qiang, *Numerical tools for modeling nonlinear integrable optics in IOTA with intense space charge using the code IMPACT-Z* in *Proceedings of the 9th International Particle Accelerator Conference*, Vancouver, Canada (2018), THPAK035.

[17] Ji Qiang, *Symplectic multiparticle tracking model for self-consistent space-charge simulation*, *Phys. Rev. Accel. Beams* **20** (2017) 014203.

[18] K. Sonnad and J. Cary, *Near equilibrium distributions for beams with space charge in linear and nonlinear periodic focusing systems*, *Phys. Plasmas* **22** (2015) 043120.

[19] L. K. Martin *et al Can a Paul ion trap be used to investigate nonlinear quasi-integrable optics?*, *J. Phys.: Conf. Ser.* **1350** (2019) 012132.